Geophys. J. Int. (2005) **163,** 238–251 doi: 10.1111/j.1365-246X.2005.02715.x

The crustal structure beneath SE Romania from teleseismic receiver functions

T. Diehl,* J. R. R. Ritter and the CALIXTO Group

Geophysical Institute, University of Karlsruhe, Hertzstr. 16, D-76187 *Karlsruhe, Germany*

Accepted 2005 June 17. Received 2005 March 30; in original form 2004 September 27

SUMMARY

Due to vigorous Neogene geodynamic processes, including oceanic subduction, slab break-off and mountain building in the Carpathian Arc, the architecture of the lithosphere in Romania is quite complicated. To improve the knowledge about the lithosphere–asthenosphere system in this region the passive seismological CALIXTO99 experiment was conducted in 1999 in the SE part of Romania. Here we present crustal models derived from the analysis of teleseismic recordings with the receiver function (RF) method of the 120 temporarily installed stations and of the permanent GEOFON stations MLR and TIRR. The RF results extend the known crustal models which are based mainly on seismic refraction work and analysis of regional earthquakes. We apply a grid-search inversion at 30 stations and use two different error estimation methods to determine the Moho depth and the average crustal v_p/v_s ratio. The complex 3-D intracrustal structure, especially the deep sedimentary basins, distorts significantly the RF waveforms within the whole station network. This leads to ambiguous results at some stations. Our model of the Moho depth has a maximum crustal thickness in the SE Carpathian Mountains at station MLR with a depth of about 45 km and an average crustal v_p/v_s ratio of 1.79. The surrounding crust in SE Romania has a thickness of mainly 35–40 km. The RFs at MLR are characterized by clear azimuthal effects that can be correlated with the variation of the sediment thickness in the foredeep of the Carpathian Mountains. A RF waveform inversion verifies these results and gains improved 1-D *S*-wave velocity models at several stations in SE Romania.

Key words: crustal structure, Moho, receiver functions, Romania.

1 INTRODUCTION

The intensive study of the Eastern and Southern Carpathian Mountains and their intermediate-depth seismicity started after the disastrous earthquake in 1977 (Fuchs *et al.* 1979) when 1570 people died mainly in Bucharest, the capital of Romania. Since then numerous questions appeared about the cause for these strong earthquakes and the consequences for SE Romania (e.g. Wenzel *et al.* 1998, 1999). The seismicity of the region (Fig. 1) can be divided in two different types, namely the widely scattered shallow crustal seismic activity with moderate magnitudes (up to $M \sim 6$) and the intense intermediate-depth seismicity (up at least $M = 7.7$), which is concentrated in a very small area of about 40 km × 80 km and a depth range between 60 and 180 km (Oncescu & Bonjer 1997; Oncescu *et al.* 1999). In this area, called the Vrancea source zone (Fig. 1), the moment magnitudes can reach at least $M_w \sim 7.7$ (e.g. in 1940 November). These earthquakes represent a major potential hazard for the whole region, especially for the metropolitan area of Bucharest that is built on relatively unconsolidated sediments. The intermediate-depth seismicity (Fig. 1, inset) is separated from the crustal events by a transition zone with only weak seismicity between about 40 and 60 km depth (Fuchs *et al.* 1979; Oncescu *et al.* 1999).

Several tomography studies revealed an isolated body with high seismic velocity in the upper mantle underneath the Vrancea region (e.g. Oncescu *et al.* 1984; Fan *et al.* 1998; Wortel & Spakman 2000). This anomaly is interpreted as subducted and detached oceanic lithosphere (Wenzel *et al.* 1998; Sperner *et al.* 2001). The subduction-related stresses have been identified as the source of the intermediate-depth seismicity. Nevertheless, there are still a lot of uncertainties concerning, for example, the coupling between crust and slab as well as the spatial dimension of the sinking slab.

For a better understanding of the Vrancea earthquakes detailed investigations of the crustal and uppermost mantle structures are conducted within the framework of the Collaborating Research Centre 461 'Strong Earthquakes—a Challenge for Geosciences and Civil Engineering' at the University of Karlsruhe (Germany) in close cooperation with the Romanian Group for Vrancea Strong Earthquakes at the Romanian Academy in Bucharest (Wenzel *et al.* 1998). In 1999, the VRANCEA99 seismic refraction project was conducted, in order to study the crust (Hauser *et al.* 2001;

*Now at: Institute of Geophysics, ETH Hoenggerberg, CH-8093 Zurich, Switzerland. E-mail: diehl@tomo.ig.erdw.ethz.ch

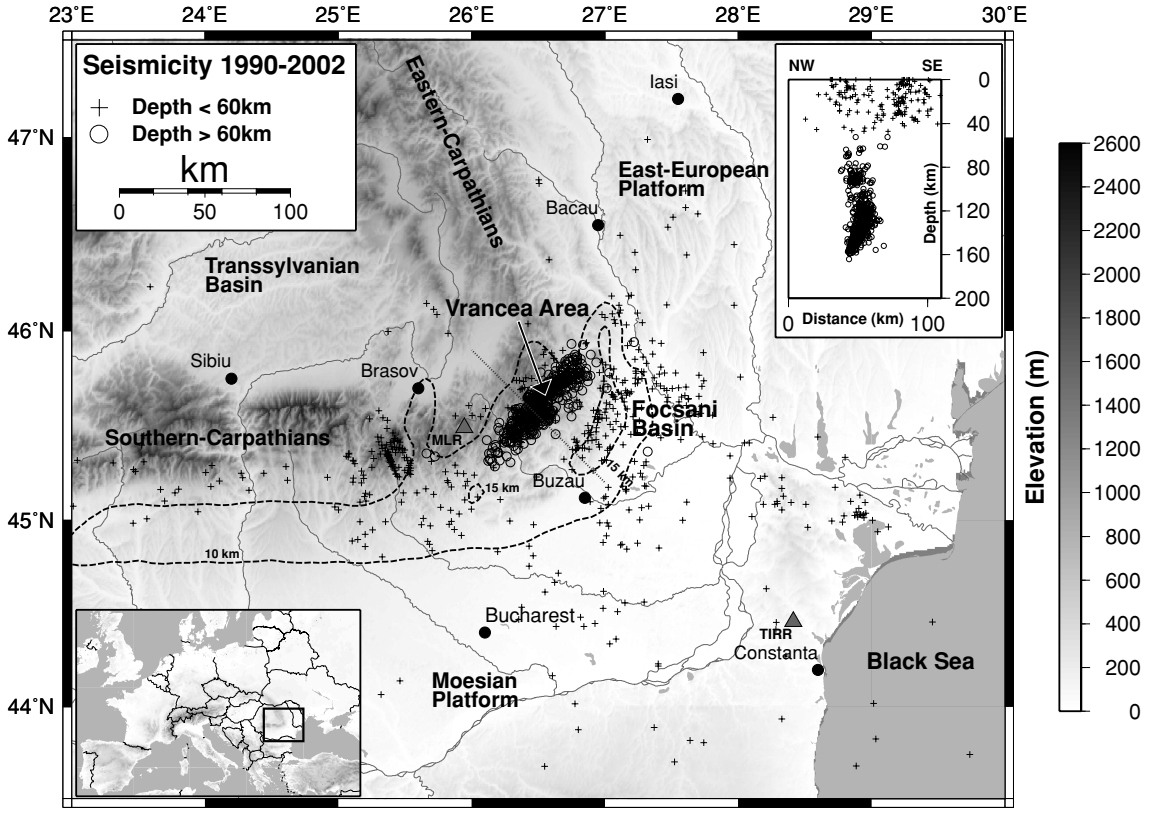

Figure 1. Distribution of the seismicity in SE Romania with earthquakes hypocenters by Oncescu & Bonjer (1997) and updates. Crustal events (crosses) are widely scattered over the region, whereas the intense intermediate-depth seismicity (circles) is concentrated in the Vrancea zone, at the SE bend of the Carpathian Arc. The inset with the vertical NW–SE cross-section through this region (dotted line in map) shows the hypocentre distribution with depth. The depth to the crystalline basement in the range of the foredeep is indicated by the 10-km and 15-km contour lines (dashed lines). MLR and TIRR are broad-band stations of the GEOFON network (triangles).

Raileanu *et al.* 2004, 2005). The 320-km-long profile traversed the Vrancea zone in NNE–SSW direction (Fig. 2). This line was followed by the VRANCEA2001 seismic refraction experiment in 2001 (Hauser *et al.* 2002), which extend over 400 km in WNW–ENE direction (Fig. 2). The *P*-wave models for both profiles indicate a Moho depth of around 40 km and the absence of a distinct crustal thickening underneath the Carpathian Mountains. Towards the Moesian Platform (Fig. 1) in the SW part of the VRANCEA99 profile, the Moho depth decreases to about 30 km. The seismic refraction models contain locally very thick sedimentary layers (15–20 km) in the foredeep, in particular in the Focsani basin (Fig. 1), which had also been mapped before (Polonic 1996).

Previous investigations of the crustal structure were conducted with seismic reflection and refraction measurements (e.g. Raileanu *et al.* 1994). Enescu *et al.* (1992) derived empirical crustal velocity–depth functions for *P* and *S* waves with local earthquake studies. A map of the crystalline basement was compiled by Polonic (1996) from a large amount of geological and geophysical data, including borehole information and seismic profiles. These models were combined by Martin *et al.* (2005) to a 3-D crustal model for SE Romania.

From 1999 May until November the passive seismological experiment CALIXTO99 (**C**arpathian **A**rc **LI**thosphere **X-TO**mography) was conducted in SE Romania (Martin *et al.* 2005). The aim of CALIXTO99 was the recording of local and teleseismic events in order to determine the structure of the lithosphere and upper asthenosphere. During the experiment 120 mobile recording stations, including 24 broad-band (BB) sensors (Streckeisen STS-2 and Güralp 40T and T3), were installed with an average spacing of about 20 km in the Vrancea zone and about 30 km at the edges of the network (Fig. 2). The whole network covered about 300 km in E–W extension and 400 km in N–S extension and recorded mostly with 20 and 50 samples per second. In addition, the data of the GEOFON (Hanka & Kind 1994) BB stations Muntele Rosu and Tirgusor (MLR and TIRR, triangles in Fig. 2) are available which are situated in the SE part of the Carpathian Arc (MLR) and close to the Black Sea (TIRR). We analyse these data sets with the receiver function (RF) method, in order to determine Moho depths, crustal v_p/v_s ratios and shear wave velocity models underneath the CALIXTO99 stations, TIRR and MLR. Our results complement and extend the existing 2-D crustal models from the seismic refraction experiments to 3-D.

2 DATA

The CALIXTO99 data set consists of three-component recordings of local, regional and teleseismic earthquakes from 1999 May to November. We select 20 teleseismic events with epicentral distances between 30° and 95°, body wave magnitudes greater than 5.0 and a signal-to-noise ratio greater than 3 for the *P*-wave pulse. Most epicentres are situated along the northern Pacific rim (Fig. 3) and arrive with backazimuths (BAZs) between 0° and 135° at the CALIXTO99 network. Fig. 2 shows all CALIXTO99 stations with RF waveforms

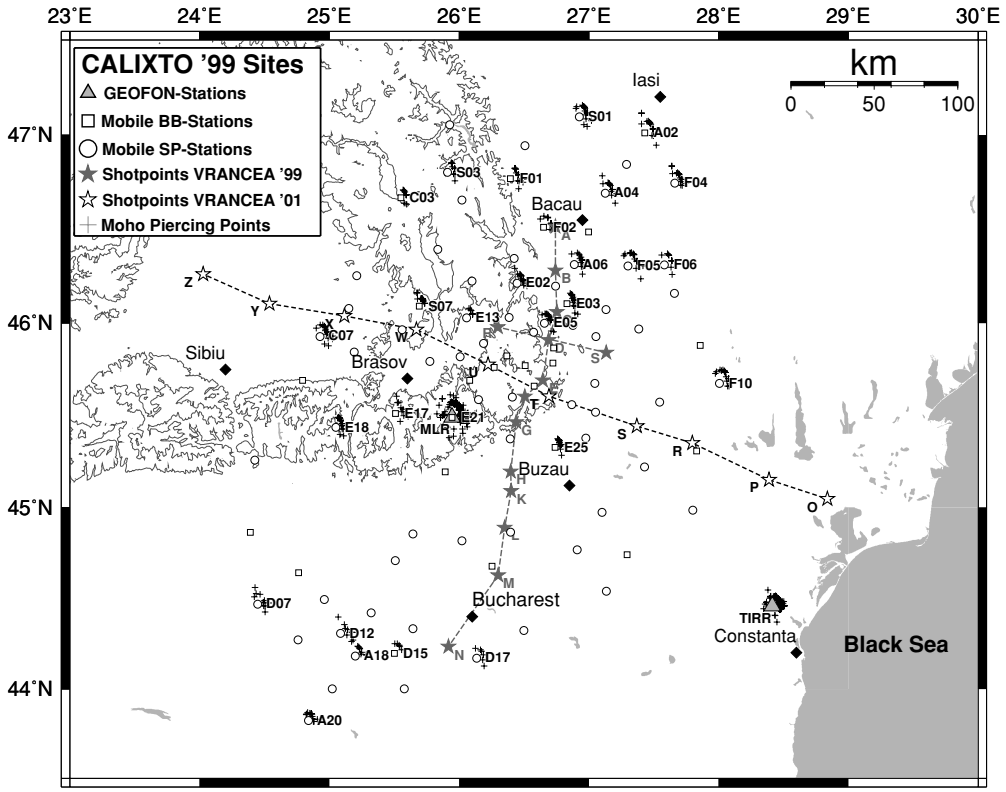

Figure 2. Location map of the broad-band (squares) and short-period (circles) stations of the CALIXTO99 experiment and the GEOFON BB-stations MLR and TIRR. Only the labelled stations could be used for a determination of the Moho depth with receiver functions; related piercing points at the Moho are given as crosses. The shot points of the two seismic refraction lines VRANCEA99 and VRANCEA2001 are marked by asterisks and letters (A–Z). The Vrancea zone is located approximately at the intersection of both lines.

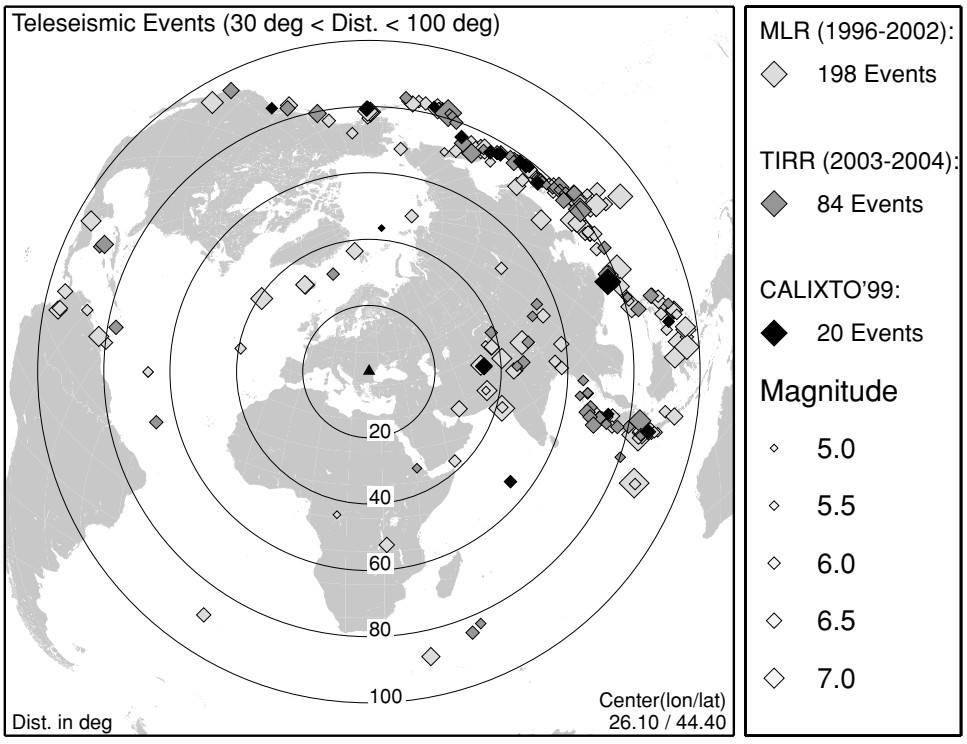

Figure 3. Distribution of the teleseismic earthquakes used in this study. The light/dark grey symbols show the events recorded by the permanent GEOFON stations MLR/TIRR between 1996 and 2004, the black symbols mark the earthquakes during the CALIXTO99 experiment. The map is centred on the CALIXTO99 network (triangle) at 26.1°E and 44.4°N.

of sufficient quality. The stations with reasonable inversion results based on a good waveform fit of major arrivals are labelled. The events from the same period of 7 months (CALIXTO99 period) are studied at the GEOFON station MLR. These results at MLR are then compared with data from a much longer recording period of 6 yr (1996–2002) in order to check the stability of the method and the results. For this comparison the waveforms of 198 events are used (Fig. 3). From the new GEOFON station TIRR we could use 84 teleseismic events.

3 METHODS

3.1 Receiver functions

The RF method is based on the coupling between *P* and *SV* waves and their conversion at seismic velocity discontinuities (e.g. Moho) underneath a seismic station (e.g. Vinnik 1977; Kosarev *et al.* 1999). We use teleseismic wavefields and analyse the *P*-to-*S* conversion at the Moho (*Ps*) and their reverberating phases in the crust. The crustal thickness and the average v_p/v_s ratio are determined by the grid-search inversion after Zhu & Kanamori (2000). In order to verify the stability and the reliability of the results, we extend this method by a bootstrapping test and also perform a chi-square-like error estimation. Subsequently, we calculate synthetic RF waveforms with a plane wave approximation (Kind *et al.* 1995) and obtain improved shear wave velocity–depth functions by iterative waveform modelling and inversion.

The pre-processing of the teleseismic waveform data and the calculation of the RFs is done according to Yuan *et al.* (1997). The first step is the deconvolution of the raw ground velocity seismogram to true ground displacement. For short period (SP) sensors as the Mark L4 seismometers with 1 s eigenperiod we applied a simulation filter with 15 s eigenperiod to amplify the transfer function at low frequencies (Scherbaum 2001). All BB and SP data are filtered with a fourth-order Butterworth bandpass filter from 0.5–12 s. After this pre-processing the seismometer components Z, N–S and E–W are rotated into the ray coordinate system L, Q and T (Plešinger *et al.* 1986) using the theoretical BAZ and rayparameter of the events. This rotation separates the different wave components. In case of an isotropic and flat layered medium L, Q and T components contain only *P*, *SV* and *SH* wave motions, respectively. The subsequent deconvolution of the Q component with the *P* wavelet on the L component removes the source function from the converted arrivals, and thus the RF for different events at a single station become comparable and can be summed to increase the signal-to-noise ratio. We apply a distance-dependent moveout correction to an average distance of 67° before the stacking. A visual inspection of the waveforms is done to sort out noisy traces or traces with disturbances in front of the *P*-wave arrival, before accepting the final radial RFs.

3.2 Grid search for Moho depth and v_p/v_s ratio

To estimate the Moho depth H and the average v_p/v_s ratio κ of the crust below a station, we apply the grid-search method after Zhu & Kanamori (2000) which is valid for horizontal layering. This method uses the delay times of the direct Moho-converted phase (*Ps*) plus its multiply reverberated crustal phases *PpPs* and *PpSs* + *PsPs*. These three phases are weighted with factors w_i (i = 1–3), which have normalized values of 0.55, 0.27 and 0.18, respectively. Here the multiples are weighted more than in Zhu & Kanamoris's (2000) study, because the *Ps* phase is often deformed by sedimentary phases. The stack function $S(H, \kappa)$ and its maximum give the best fitting value for the model parameters H and κ. As input parameter the average crustal *P*-wave velocity $\langle v_p \rangle$ must be estimated as stacking velocity. This unknown parameter is taken either from the two recent seismic refraction lines or from local Romanian earthquake studies (Enescu *et al.* 1992) in our case (see below).

The result of the $H-\kappa$ grid search contains several uncertainties: the variance of the data due to seismic noise, lateral heterogeneities and the uncertainty of the input parameter $\langle v_p \rangle$. The determination of the model errors due to the data variance is quite difficult and often related errors for H and κ are given (for a discussion of such problems see Julià & Mejía (2004)). Therefore, we focus on the stability and errors of our RF stacks with relatively few ($\leq$20) recordings which are a typical amount for temporarily deployed networks. For this purpose two different methods are applied: a bootstrap-resampling technique and a chi-square-like error estimator.

3.3 Bootstrap resampling

To estimate the uncertainties of $S(H, \kappa)$ due to the variability of the individual RFs we use the bootstrap resampling technique (e.g. Davison & Hinkley 1997) which was also applied to RF for example, by Julià & Mejía (2004) or Dugda *et al.* (2005). The key concept of this technique is that the original set of N data points (RF traces) is resampled to form a large number of L 'sub'-data sets (ensembles). The different grid-search results $(H_i, \kappa_i, i = 1, \ldots, L)$ of these ensembles are used to calculate the variance of the model parameters and reflect the stability of the stack function. By calculating the standard deviation for the model parameters (H, κ) and their correlation coefficient r we can determine the 1σ error ellipse ($\sim$standard deviation) in the $H - \kappa$ domain:

$$\sigma_H^{\mathrm{Boot}} = \left[\frac{1}{L-1} \sum_{i=1}^{L} (H_i - \overline{H})^2 \right]^{1/2}, \quad \text{with } \overline{H} = L^{-1} \sum_i H_i, \quad (1)$$

$$\sigma_\kappa^{\mathrm{Boot}} = \left[\frac{1}{L-1} \sum_{i=1}^{L} (\kappa_i - \overline{\kappa})^2 \right]^{1/2}, \quad \text{with } \overline{\kappa} = L^{-1} \sum_i \kappa_i, \quad (2)$$

$$r = \frac{\sigma_{H\kappa}^2}{\sigma_H^{\mathrm{Boot}} \sigma_\kappa^{\mathrm{Boot}}}, \quad \text{with } \sigma_{H\kappa}^2 = \frac{1}{L-1} \sum \left(H_i - \bar{H}\right)(\kappa_i - \bar{\kappa}). \quad (3)$$

The resampling process is done according to Tichelaar & Ruff (1989): a bootstrap ensemble is a random selection of n RF traces out of N original RF traces. Such an ensemble may contain a certain RF trace more than once. Usually the bootstrap resampling is done with $n = N =$ const to estimate σ_{H} and σ_κ. Subsampling such as the jackknife method (Davison & Hinkley 1997) with variations of n from N to 1 can be done to study the dependency of $\overline{H}$, $\overline{\kappa}$, σ_{H}, σ_κ and r on n.

The amount L of ensembles is a free parameter. It controls more or less the smoothness of the result. L should be chosen as a compromise between an adequate smooth model distribution and an appropriate computation time. We tested values between 10 and 500, where the later represents the best compromise. In the case of very sparse data sets we expect a failure of this technique, because the different ensembles are no longer a random selection.

3.4 Chi-square-like error estimator

The misfit between model-predicted data and measured data can be expressed by the chi-square function (Bevington & Robinson 1992).

In our case the chi-square estimate is measured as the traveltime difference between the predicted arrival time of a conversion phase in the RF from a reference model and the arrival time of a phase in the measured RF trace in our case. The reference model corresponds to the Zhu & Kanamori (2000) grid-search result derived from the stack of all RF traces at the corresponding station. This time difference or absolute error of each RF phase (*Ps*, *PpPs*, . . .) is weighted as in the original grid search (see above). The performance of the chi-square method strongly depends on the quality of the RF trace. If a phase cannot clearly be identified, it is weighted with 'zero'. The arrival times in the reference model are: $T_{ij}\,(H, \kappa, p_i, v_p)$ (with $i = 1, \ldots, N$; $j = 1$–3 and p_i ith slowness) for the three phases. The picked arrival times in the measured RF are t_{ij}. We get traveltime residuals from $d_{ij} = t_{ij} - T_{ij}$ and the weighting factors w_{ij}. The weighted standard deviation for the jth phase is defined as (e.g. Bevington & Robinson 1992):

$$\sigma_j^w = \sqrt{\frac{\sum_{i=1}^{N} w_{ij} d_{ij}^2}{\sum_{i=1}^{N} w_{ij}} \cdot \frac{N'}{N'-1}}, \tag{4}$$

with N': number of elements with $w_{ij} \neq 0$. In this way we determine an 'error interval' for each of the three converted phases. Subsequently, we determine the solution couples of H and κ with a specific $\langle v_p \rangle$, which fall into the error intervals by the grid search after Zhu & Kanamori (2000).

3.5 Uncertainty of stacking velocity $\langle v_p \rangle$

The average crustal stacking velocity $\langle v_p \rangle$ is determined by vertically averaging of existing seismic velocity models from local earthquake studies or seismic refraction work. For SE Romania we find $5.8\,\mathrm{km\,s^{-1}} \leq \langle v_p \rangle \leq 6.3\,\mathrm{km\,s^{-1}}$ (see Table 1). A comparison of the seismic refraction models (CSS) and the local earthquake models (PSS) of Enescu *et al.* (1992) and Raileanu *et al.* (1998) suggests a variability of the average crustal *P*-wave velocity of at least $\pm 0.2\,\mathrm{km\,s^{-1}}$ (Table 1). This value may be too large for stations situated close to the seismic refraction profiles, but it appears reasonable for CALIXTO99 stations off the profiles. We study the influence of the uncertainty of the stacking velocity $\langle v_p \rangle$ on the $H - \kappa$ result by variations of $\langle v_p \rangle$ within realistic bounds (6.0–6.4 km s^{-1}). Therefore, we perform the bootstrap and chi-square analysis separately for three different plausible $\langle v_p \rangle$ (6.0, 6.2 and 6.4 km s^{-1}) to estimate the influence of $\langle v_p \rangle$ on H and κ.

3.6 Waveform modelling and *S*-velocity structure

To test the results of the grid-search analysis and to extract more information from the RF trace, we apply the *S*-wave velocity (v_s) inversion after Kind *et al.* (1995). This technique is based on a plane wave approximation and fits the synthetic RF waveform obtained from a starting model to the measured (stacked) RF by adjusting

Table 1. Station name, station latitude, station longitude, number of RF traces, estimated v_p/v_s ratio κ, Moho depth H and their error estimations with the bootstrap and the chi-square methods. For stations close to one of the two recent CSS profiles (Hauser *et al.* 2002), resulting Moho depth, average crustal v_p/v_s ratio and $\langle v_p \rangle$ (Raileanu *et al.* 2005) are given. Letters in parentheses indicate the nearest CSS shotpoint (see Fig. 2). The $\langle v_p \rangle$ values resulting from the CSS profiles are also compared with those derived from passive source seismology (PSS) (Raileanu *et al.* 1998; Enescu *et al.* 1992).

Stat.	Lat. (°)	Lon. (°)	No. of traces	Bootstrap κ	Bootstrap H (km)	Chi-Square κ	Chi-Square H (km)	CSS H (km)	CSS κ	CSS $\langle v_p \rangle$	PSS km s^{-1}
MLR	45.4920	25.946	198	1.79 ± 0.01	45.1 ± 1.4	1.79 ± 0.04	45.0 ± 1.5	41.4 (G)	1.75	5.9	6.2
MLR	45.4920	25.946	20	1.75 ± 0.03	45.7 ± 1.6	1.75 ± 0.04	46.0 ± 1.8				
TIRR	44.4581	28.413	84	1.63 ± 0.05	35.2 ± 1.6	1.63 ± 0.05	35.5 ± 1.1				
A02	47.0108	27.430	15	1.69 ± 0.06	39.3 ± 2.0	1.71 ± 0.04	39.0 ± 0.7				
A04	46.6938	27.125	15	1.89 ± 0.03	35.2 ± 2.6	1.88 ± 0.05	35.0 ± 0.6				
A06	46.3148	26.887	14	1.87 ± 0.10	38.4 ± 5.3	1.89 ± 0.07	37.1 ± 0.9	38.7 (B)	1.75	6.2	6.2
A18	44.1840	25.198	9	1.80 ± 0.04	33.5 ± 1.9	1.78 ± 0.05	34.5 ± 0.6				
A20	43.8250	24.838	12	1.80 ± 0.02	27.5 ± 1.2	1.80 ± 0.07	27.5 ± 0.8				
C03	46.6685	25.551	10	1.78 ± 0.05	27.1 ± 1.6	1.78 ± 0.10	27.2 ± 2.1				
C07	45.9288	24.926	17	1.79 ± 0.07	37.6 ± 3.2	1.76 ± 0.08	38.4 ± 1.3	34.0 (X)	–	6.1	6.1
D07	44.4700	24.445	11	1.79 ± 0.13	35.3 ± 7.0	1.86 ± 0.05	32.5 ± 0.7				
D12	44.3080	25.086	8	1.87 ± 0.06	35.0 ± 2.7	1.86 ± 0.08	35.0 ± 1.1				
D15	44.1960	25.501	5	1.82 ± 0.08	36.5 ± 4.9	1.85 ± 0.07	35.0 ± 1.0				
D17	44.1707	26.135	6	1.85 ± 0.02	32.8 ± 1.2	1.86 ± 0.05	32.5 ± 0.7	32.1 (N)	1.75	6.2	6.2
E02	46.2132	26.446	17	1.64 ± 0.04	31.3 ± 1.7	1.65 ± 0.07	31.5 ± 1.0				
E03	46.1033	26.831	17	1.92 ± 0.03	35.8 ± 1.4	1.91 ± 0.06	35.7 ± 1.0	39.4 (C)	1.75	6.1	6.2
E05	46.0002	26.656	14	1.86 ± 0.07	32.4 ± 3.4	1.88 ± 0.07	31.2 ± 1.0	39.4 (C)	1.75	6.1	6.2
E13	46.0297	26.055	7	1.83 ± 0.13	31.7 ± 4.5	1.72 ± 0.07	34.0 ± 1.0	34.0 (U)	–	5.9	6.2
E17	45.5122	25.508	9	1.70 ± 0.11	38.1 ± 3.6	1.68 ± 0.09	39.0 ± 1.4				
E18	45.4370	25.049	17	1.69 ± 0.07	35.3 ± 3.2	1.68 ± 0.09	35.4 ± 1.3				
E21	45.4910	25.945	15	1.79 ± 0.04	45.0 ± 1.6	1.77 ± 0.06	45.5 ± 1.1				
E25	45.3272	26.738	16	1.83 ± 0.04	30.4 ± 1.7	1.81 ± 0.08	31.0 ± 0.9	39.8 (T)	–	5.8	6.2
F01	46.7698	26.395	14	1.85 ± 0.07	38.0 ± 3.7	1.83 ± 0.06	38.5 ± 0.9				
F02	46.5117	26.649	10	1.71 ± 0.10	37.3 ± 5.9	1.74 ± 0.08	34.9 ± 1.1	38.1 (A)	1.76	6.3	6.2
F04	46.7468	27.660	15	1.81 ± 0.05	34.4 ± 2.0	1.80 ± 0.09	34.9 ± 1.2				
F05	46.3073	27.299	17	1.79 ± 0.07	43.2 ± 4.2	1.84 ± 0.10	40.6 ± 1.5				
F06	46.3122	27.579	9	1.85 ± 0.08	37.2 ± 5.1	1.89 ± 0.07	33.6 ± 0.9				
F10	45.6760	28.004	17	1.62 ± 0.08	43.3 ± 3.8	1.61 ± 0.06	44.3 ± 1.3				
S01	47.0972	26.926	18	1.81 ± 0.10	36.6 ± 5.8	1.83 ± 0.08	34.9 ± 1.1				
S03	46.8045	25.909	12	1.73 ± 0.08	36.0 ± 4.7	1.71 ± 0.07	34.5 ± 1.1				
S07	46.0903	25.692	14	1.67 ± 0.03	27.6 ± 1.5	1.68 ± 0.09	27.4 ± 1.1	34.0 (W)	—	6.1	6.1

the v_s model. During the inversion the number of layers and the depth of layer boundaries is kept fixed. These parameters may be adapted by trail and error to improve the waveform fit. As starting models we take the result from the grid search (H) and the gross crustal structure along the available seismic refraction profiles. A problem of this inversion technique is the ambiguity of the results, mainly in the case of complex waveforms due to strong crustal heterogeneity like 3-D varying sedimentary layers or dipping interfaces.

4 RESULTS

Starting with the analysis of the radial RFs from station MLR, we verify the stability of the results by a comparison of the model parameters derived from the data of the 7 months CALIXTO99 period with the data set containing 6 yr of recordings. Based on this test the RFs at the CALIXTO99 stations are studied.

4.1 Station MLR

In Fig. 4 we present the RFs at MLR as function of the BAZ. The conversion phases from the sediment–basement boundary at around 0.5 s delay time are clearly visible as positive (black) phase, indicating a negative velocity contrast for an incident wavefield from below. The conversion phases from the Moho follow at 4–6 s delay time with an apparent sharp time-shift from 5.8 s to 4.1 s at a BAZ of ∼70°. Other time shifts for the apparent Moho conversion phases are visible at BAZs of ∼180° and ∼315°. Thus similar crustal RF are obtained at BAZ intervals between 315–70°, 70–180° and 180–315°. Obviously, significant lateral variations in crustal structure cause these changes in the waveforms. The transverse RFs (not shown here) contain several phases which also denote non-plane layering below MLR.

The results of the $H - \kappa$ grid search at MLR are shown in Fig. 5 for different cases, including a comparison of the stability of the results based on the two data sets and the two different techniques for error estimation. The 1σ error ellipse corresponds to the standard deviations of the parameters and their correlation. Using the data from the CALIXTO99 recording period (20 RF traces), we determine a Moho depth H of 45.7 km and an average crustal v_p/v_s ratio κ of 1.75 (Fig. 5a). For a constant stacking velocity $\langle v_p \rangle = 6.2$ km s^{-1} the bootstrap resampling in Fig. 5(a) yields standard deviations of $\sigma_H = \pm 1.0$ km and $\sigma_\kappa = \pm 0.03$. The black dots in Fig. 5(a) represent solutions of the grid search for the $L = 500$ random ensembles, mostly the solutions plot on each other. The normalized frequency of the solutions is displayed by the grey shading, and the mean values for κ and H are indicated by the black cross. The 1σ uncertainties for both parameters are indicated by the ellipses, calculated from

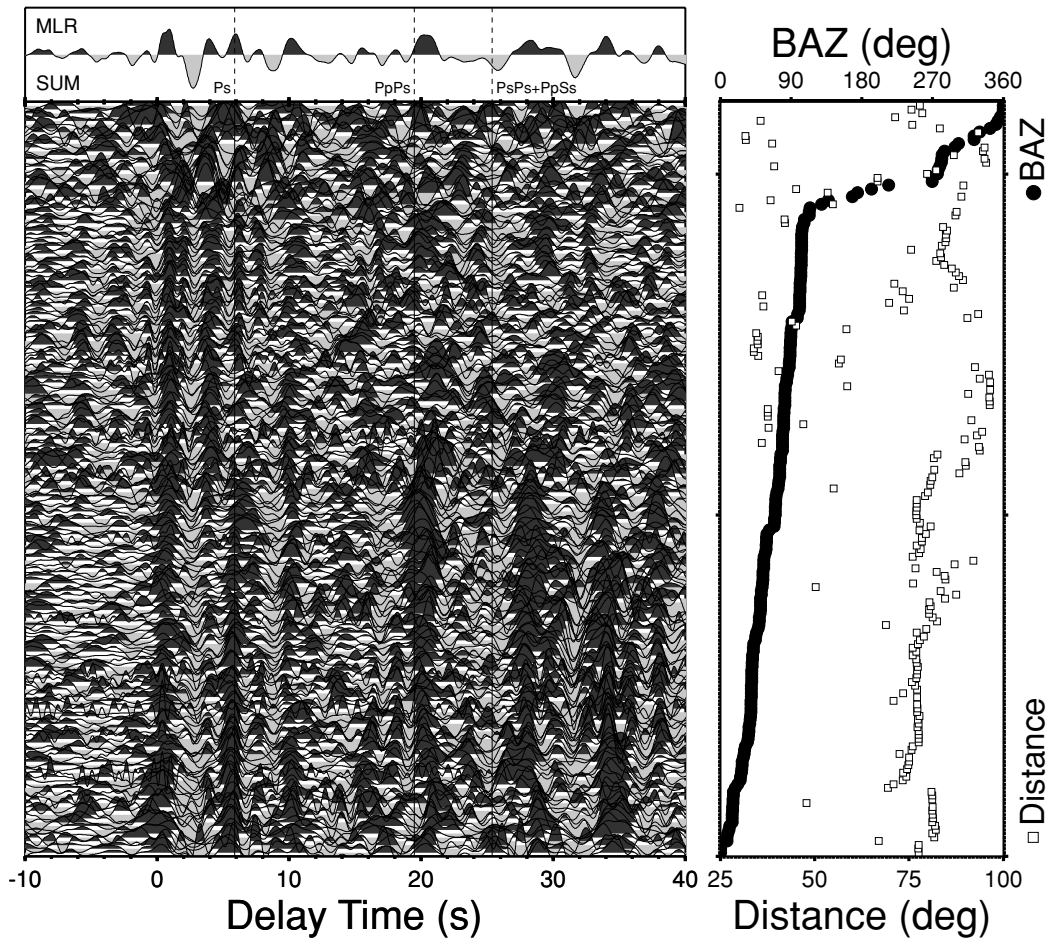

Figure 4. A total of 198 radial receiver functions of the GEOFON broad-band station MLR. In the stacked trace at the top the Moho *Ps* phase and its multiples are shown as expected from the best-fitting model (Fig. 5). A distance-dependent moveout correction is applied for the *Ps* phase. The backazimuth (black dots) and the epicentral distance (open squares) of the sources are shown at the right. At around 70° BAZ there is a clear change in the waveforms of the receiver functions. Further changes are visible at 180° and 315°.

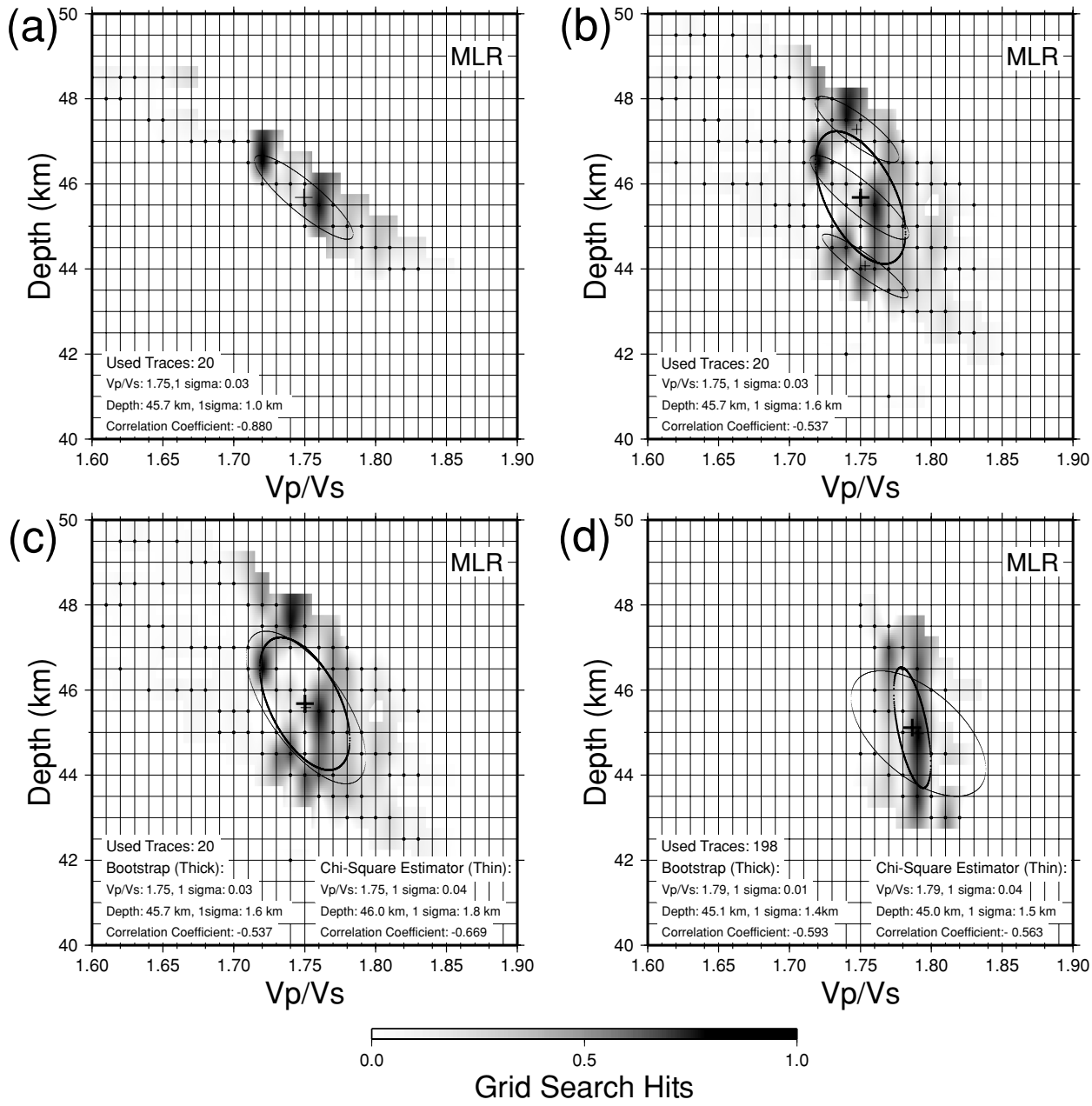

Figure 5. Result of the grid search with 500 bootstrap ensembles for station MLR (20 RF traces in (a)–(c) and 198 RF traces in (d). Black dots represent a grid-search hit. The normalized frequency of hits is shown by the grey code. The mean for v_p/v_s and the Moho depth is indicated by black crosses, the 1σ uncertainty is given through ellipses. (a) Result for fixed stacking velocity of 6.2 km s^{-1} and 20 RF. (b) Result for stacking velocities of 6.0, 6.2 and 6.4 km s^{-1}. The thin ellipses and crosses represent the single results, the thick one the combined result. (c) Comparison between bootstrap and chi-square error estimations at variable stacking velocities (6.0, 6.2 and 6.4 km s^{-1}) and 20 RF. (d) same as (c) with 198 RF.

the mean values of H and κ, σ_H, σ_κ and the correlation coefficient r following eqs (1)–(3). In Fig. 5(b) we varied the stacking velocity $\langle v_p \rangle$ from 6.0 km s^{-1} to 6.4 km s^{-1} in steps of 0.2 km s^{-1}. The thin crosses and ellipses represent H and κ solutions and their 1σ intervals for the three solutions which mainly lead to a greater Moho depth for increasing $\langle v_p \rangle$. The combined 1σ region for the three $\langle v_p \rangle$ is shown by the thick line. The variation of $\langle v_p \rangle$ affects preferentially only the error of H, which becomes ± 1.6 km. Fig. 5(b) demonstrates that a small uncertainty as 0.2 km s^{-1} for $\langle v_p \rangle$ leads to an uncertainty of the Moho depth, which is as large as the uncertainty due to the variation of the single RF traces. Thus a good estimate of $\langle v_p \rangle$ is necessary for reliable results.

The comparison of the bootstrap resampling technique (BT) and the chi-square estimator (CE) is shown in Fig. 5(c) for different $\langle v_p \rangle$ and 5(d) for different numbers of RF traces. In the case of 20 RF traces both methods gain similar values for the mean model parameters which are within similar standard deviations (Fig. 5c: $H = 45.7 \pm 1.6$ km and $\kappa = 1.75 \pm 0.03$ for BT compared to $H = 46.0 \pm 1.8$ km and $\kappa = 1.75 \pm 0.04$ for CE). In Fig. 5(d) the nearly identical results and error estimates for 198 RF are displayed

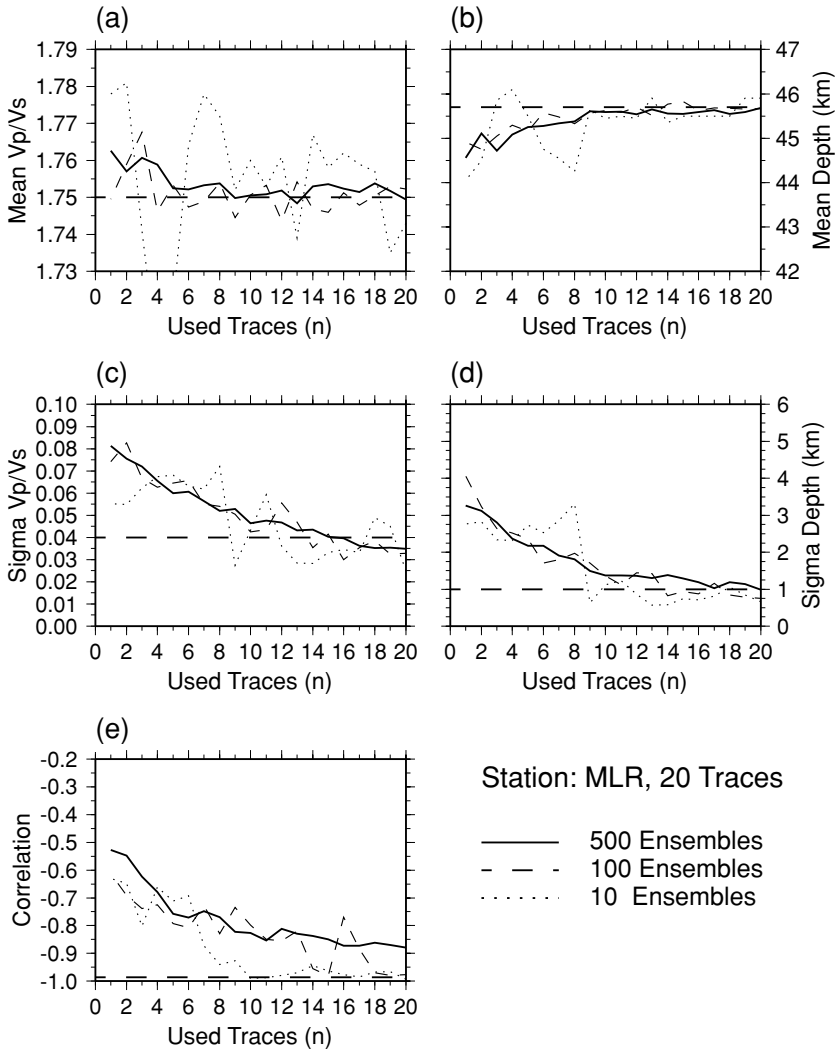

Figure 6. Bootstrap results as function of n and L for station MLR. The dashed horizontal line represent the result of the chi-square estimator for all traces. (a) v_p/v_s ratio κ, (b) Moho depth, (c) σ_κ, (d) σ_H and (e) correlation coefficient r.

($H = 45.1 \pm 1.4$ km and $\kappa = 1.79 \pm 0.01$ for BT compared to $H = 45.0 \pm 1.5$ km and $\kappa = 1.79 \pm 0.04$ for CE). Compared to the results in Figs 5(a) and (c) (20 RF), the much lower amount of RFs there seems to be enough to achieve well-constrained results.

The dependency of the bootstrap estimation from the number of used events (n) and the amount of ensembles (L: 10, 100 and 500) is displayed in Fig. 6. As maximum n we choose 20, because this is a typical amount of RFs for a temporary station deployment. The horizontally dashed lines represent the result derived by the chi-square estimator using all 20 RFs as reference. We find that L mostly controls the smoothness of the curves but not the actual result. Between $10 < n < 20$ the results of the bootstrap analysis seem to be approximately constant, especially for the Moho depth (Figs 6b and d). For $n < 10$ the results scatter widely and clearly depend on n. Consequently, we suggest that the bootstrap method provides unreasonable results for stations with less than $\sim$10 good recordings. The chi-square estimator for $n = 20$ is in good agreement with the bootstrap analysis. For stations with less than $\sim$10 recordings it is also not stable (not shown here) and the results should be interpreted with care.

To determine an improved crustal S-wave velocity model for station MLR, we fit the measured stacked RF waveform to a synthetic RF by waveform modelling and inversion of v_s (see 3.6). In order to minimize azimuthal effects, we considered only the sum of the 20 RFs from the CALIXTO99 recording period, which contains events with azimuthal directions between 350° and 90° and avoids major disturbances with sedimentary phases (see Fig. 3). The measured stacked RF trace is shown in Fig. 7(a) as trace 1 and dashed in traces 2–5. The starting model (dashed line) in Fig. 7(b) is taken from Raileanu *et al.* (1998) who determined the crustal structure below MLR from geological models and traveltime data of local events. The basement, Conrad and Moho discontinuities are placed at 8, 24 and 50 km depth, respectively. The comparison between the synthetic and observed RFs (trace 2) shows a quite poor agreement. By further waveform modelling, a better fit to the data can be obtained. In the first step the result of the grid search is included, and the Moho is shifted to 45.7 km depth (trace 3). Then the depths of intracrustal discontinuities are adjusted (trace 4). Finally, we fit the amplitudes by inversion of v_s (trace 5) and obtain the best-fitting model (Fig. 7b, solid line). This v_s model is similar to the v_s model by Raileanu *et al.* (2004, 2005) along the VRANCEA99 line which is located about 50 km east. Our v_s model with a 45.7-km-thick crust does not denote a prominent crustal root for the Carpathian Mountains but only a slight increase in crustal thickness of about

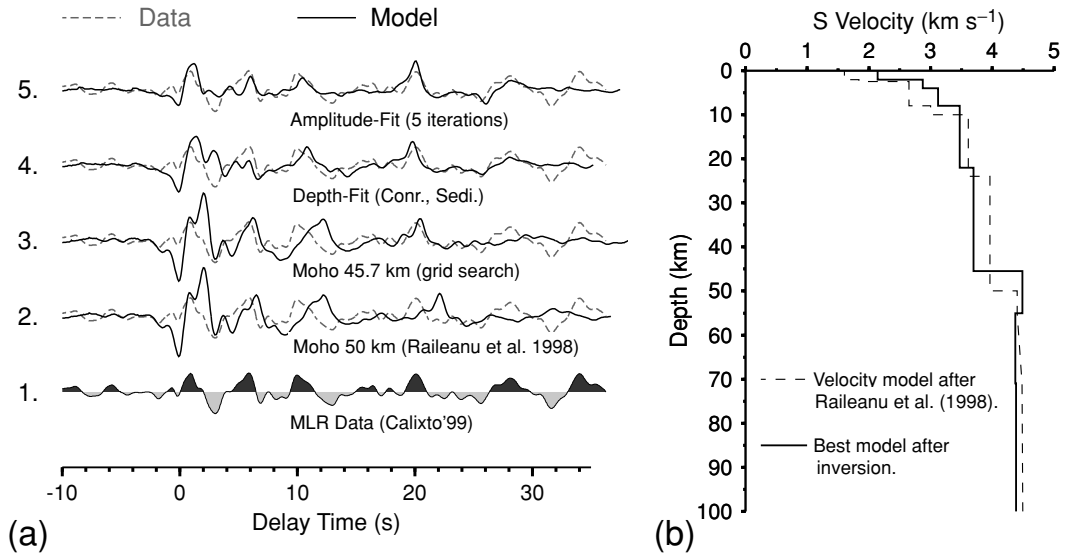

Figure 7. Synthetic modelling of the receiver function waveform at station MLR. (a) The dashed lines show the summed trace of the CALIXTO99 data (1), the solid lines represent the modelled waveform for different v_s models. The input model for trace 2 is taken from Raileanu *et al.* (1998) in (b). The input model for trace 3 has the Moho depth of the inversion after Zhu & Kanamori (2000). Trace 4 results from a better fit of the sediment thickness and trace 5 is achieved from 5 v_s iterations (best model given in (b)).

5 km relative to the surrounding region. The Conrad discontinuity is at about 20 km depth, and presumably sedimentary layers with $v_s < 3$ km s^{-1} reach down to about 5 km depth.

4.2 TIRR and CALIXTO99 stations

We apply the RF and error analyses as discussed in the last section also to the data of the new GEOFON station TIRR and the CALIXTO99 data. We obtain RF waveforms of sufficient quality for 65 CALIXTO99 stations. For 28 stations (labelled in Fig. 2) the $H-\kappa$ grid search leads to reasonable results, for the remaining stations the inversion for H and κ is spoiled mainly by interfering sedimentary phases. We observe a strong variation of the RF waveforms and their quality over the whole network. Especially in the southern part of the network, only few stations exhibit coherent RF waveforms, and only six stations are included for the $H-\kappa$ inversion there. Table 1 contains the locations of the stations used for the grid search, the number N of RF traces and the solution of the $H-\kappa$ inversion with the respective errors. In addition we compare the results of the controlled source seismology (CSS) experiments VRANCEA99/2001 with stations close to these profiles.

Fig. 8 displays radial RF examples for four CALIXTO99 stations in different tectonic regions: E03 at the eastern transition to the Carpathian Mountains, E25 in the sedimentary foreland south of the Focsani Basin, C03 in a small basin between the Carpathian Mountains and the South Harghita Mountains and F01 in the East Carpathian Mountains. The RF traces in Fig. 8 are sorted by ascending BAZ as in Fig. 4. The variation in the waveforms at the stations reflects seismic noise and mostly the local inhomogeneous geological settings with distinct 3-D structure (sediment basins, mountains, . . .). Most stations record converted phases at around 1–2 s, which can be attributed to the lower edge of the sedimentary layers or upper boundary of the crystalline basement, and at around 4 s from the Moho discontinuity.

The waveforms at station E03 exhibit a dominant sedimentary phase around 2 s (Fig. 8a). The Moho depth $H = 35$ km derived from the grid search is a bit shallower than in the seismic refraction VRANCEA99 model (Hauser *et al.* 2002) which is about 25 km west and closer to the Carpathian Mountains. The v_p/v_s ratio $\kappa = 1.95$ at E03 is quite high and higher than in the model by Raileanu *et al.* (2004). In contrast to E03, the waveform at E25 contains the first significant phase at around 4 s delay time (Fig. 8b). With an average crustal P-wave velocity of 6.2 km s^{-1}, the grid search yields a depth of 31.0 km for this conversion interface (Table 1). Assuming that this interface is the crust–mantle boundary, the result is smaller than in the seismic refraction model VRANCEA99 of Hauser *et al.* (2002), which indicates a Moho depth of about 40 km some 20 km north of station E25 (Table 1).

A small sedimentary phase can be observed at station C03 (Fig. 8c) where the most dominant converted phase has a delay between 3.5–4.0 s. This corresponds to a shallow Moho depth of 27.0 km, which also differs significantly from the seismic refraction models and may indicate a transitional region to the Transylvanian Basin. Fig. 8(d) displays the RFs at station F01 with a prominent phase from the sedimentary basis. The inverted RF waveforms yield a Moho depth of 38.5 km here, which is in good agreement with the nearby seismic refraction model (Hauser *et al.* 2002).

To derive 1-D shear wave velocity (v_s) models as well as to test and improve the grid-search results, especially at stations with unreasonable or ambiguous grid-search results (e.g. E25 and C03) RF waveform modelling was done for a more detailed analysis as described in Section 3.6. As starting model we take as *a priori* information the grid-search solutions and the available seismic refraction models. Fig. 9 shows the inversion results for the four stations whose waveforms are displayed in Fig. 8. For station E03 the initial model already yields a good agreement between the observed and synthetic RFs (Fig. 9a lower waveforms) but with lower synthetic amplitudes. The inversion of the depth-dependent v_s structure clearly improves the amplitude fit and finds a small low-velocity layer in the lower crust.

For stations like E25 and C03 we tried several different starting models, e.g. models including shallow Moho depths or deep sedimentary basin structures. For station E25 we set the Moho to 41.3 km depth and introduced an additionally interface at 16 km depth, which

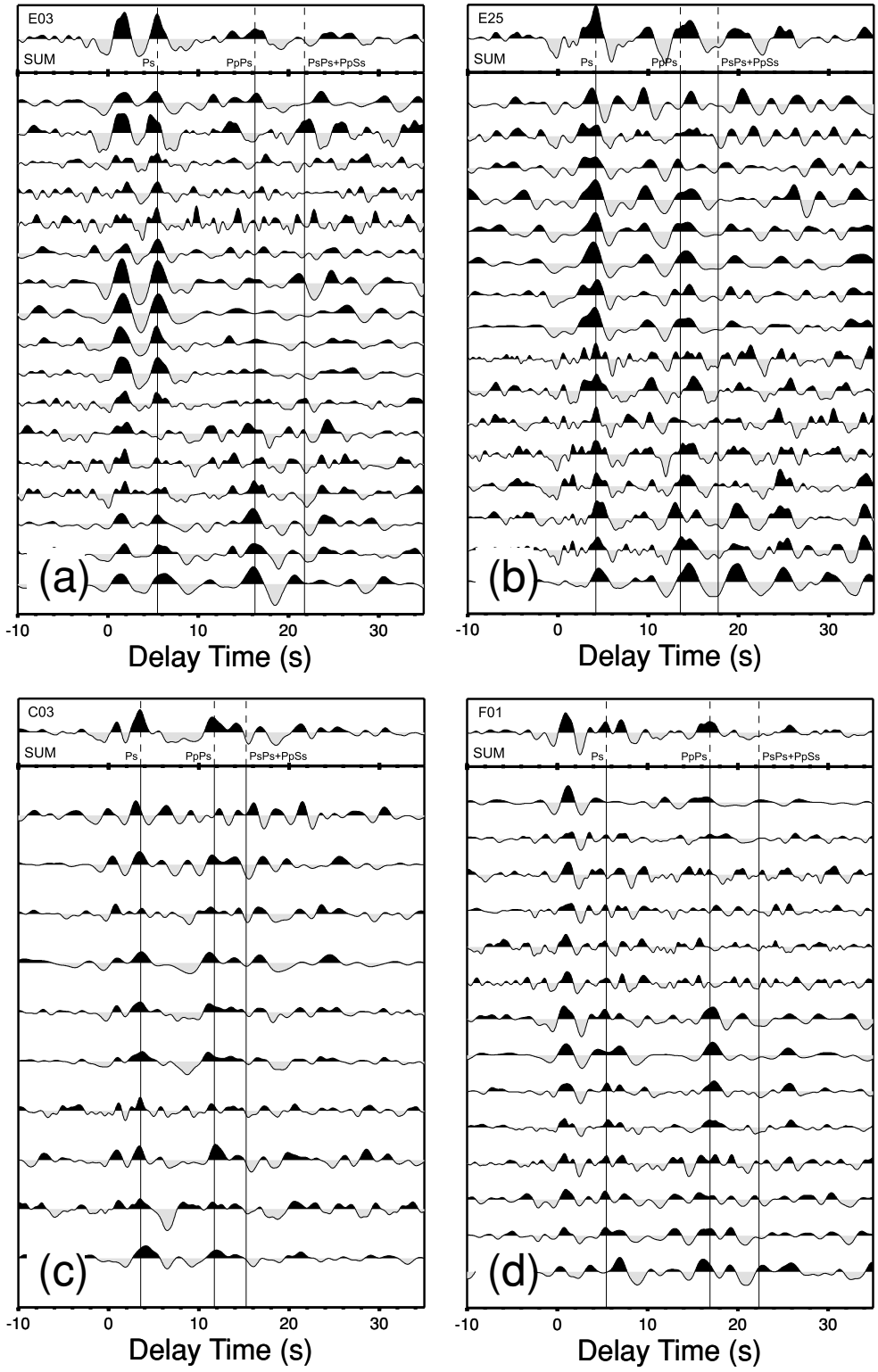

Figure 8. RF sections at four CALIXTO99 stations: (a) E03 on the eastern transition to the Carpathian Orogene), (b) E25 on a sediment region south of the Focsani Basin), (c) C03 on a small sediment basin west of the Carpathians. (d) F01 close to the East Carpathians. The traces are sorted by ascending BAZ according to Fig. 4 and the sum is displayed at the top.

stands for the lower boundary of the sedimentary trough close to the Focsani Basin. After the final inversion the velocity model at E25 suggests a dominant v_s contrast at the basement–basin transition and furthermore, the Moho structure remains as minor negative velocity contrast. This unrealistic low v_s zone at the bottom of the crust indicates a strong distortion of the Moho conversion phase by the strong sedimentary multiples and should not be used for further interpretations.

The initial v_s model for station C03 includes the Conrad discontinuity at 23 km and the Moho at 37 km depth (Fig. 9c). The final

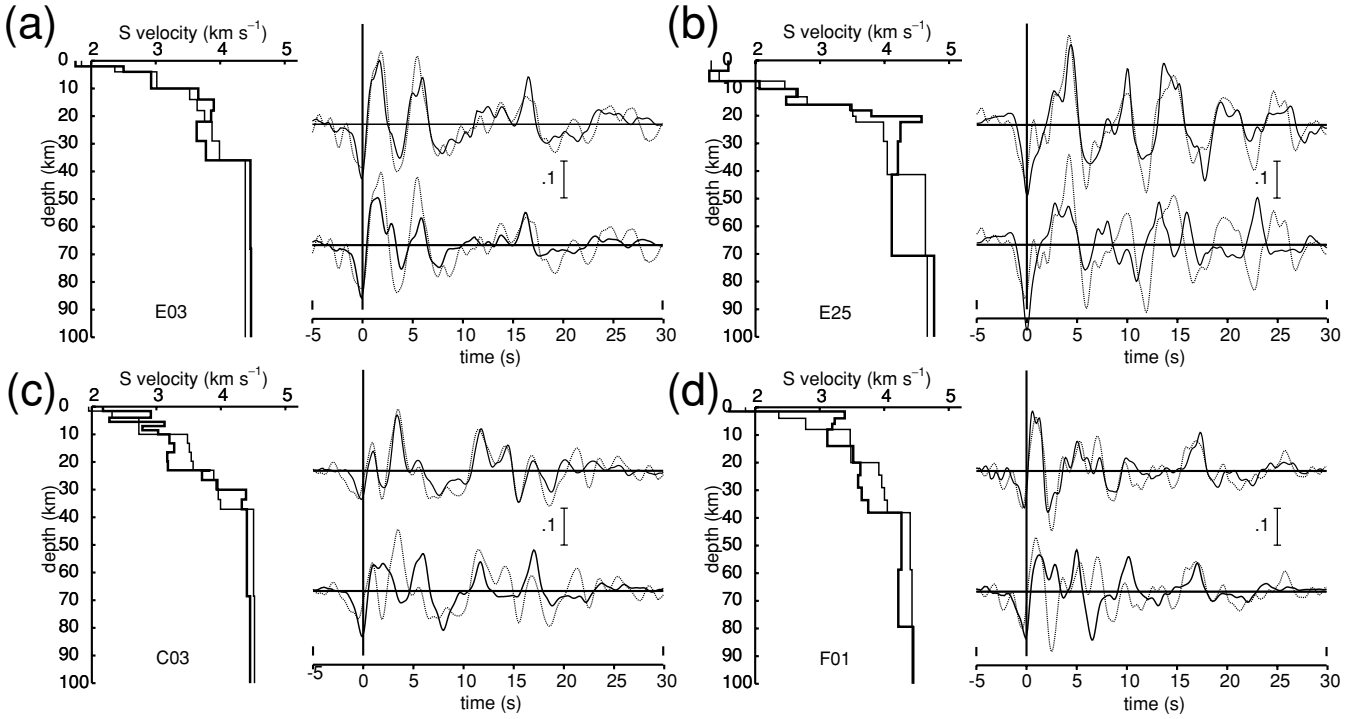

Figure 9. Examples for v_s inversion for four CALIXTO99 stations: (a) E03 (Carpathian Orogene), (b) E25 (Focsani basin), (c) C03 (Transylvanian basin) and (d) F01 (East European Platform). The traces on the right hand side represent the stacked RF data (dashed line in both plots), the synthetic RF according to the initial model (solid thin line in lower plot) and the synthetic RF according to the final model (solid thick line in upper plot). On the left hand side the *S*-wave velocity–depth function is shown as thin line for the initial and as thick line for the final model.

inverted model has a layered upper crust to explain the converted phases and the crust-mantle boundary is shifted upwards to 29 km depth, which coincides with the grid-search result. The initial v_s model for station F01 explains mostly all major phases, however, it cannot reproduce some observed additional phases (Fig. 9d). The v_s inversion results in an improved fit and confirms the crustal thickness of 38.5 km derived by the grid search (Table 1).

In general, we observe a strong influence of the initial model on the forward modelling result and v_s inversion model. Especially in the case of complex RF waveforms due to complicated layered sedimentary structures, most waveform details cannot be explained by unambiguous and 1-D-layered v_s models. In these cases several different starting models can lead to similar synthetic RF waveforms and thus prevent a unique determination of v_s from the RF waveforms alone.

The results of the $H - \kappa$ grid search for the 28 CALIXTO99 stations, TIRR, and MLR are summarized in Table 1 and in Fig. 10 and discussed below. A comparison of the outcome from the two error estimation techniques, demonstrates the consistency of the mean model parameters in both cases. At most stations the bootstrap analysis leads to a smaller error for the v_p/v_s ratio κ and to a significantly larger value for the uncertainty in H compared to the chi-square estimator result.

5 DISCUSSION AND CONCLUSIONS

The bootstrap resampling technique provides estimates on the variance of the model parameters, for example, ∼1–4 km for the Moho depth H at the CALIXTO99 stations. The variation of the unknown stacking velocity within reasonable bounds causes another error of H of about 2–4 km. Thus the resulting uncertainty due to the error of $\langle v_p \rangle$ is about the same as the error related to the data variance. Therefore, a good knowledge of $\langle v_p \rangle$ is necessary for a proper determination of the crustal thickness. The bootstrap method leads to unstable results for H and κ as well as large errors in case of small data sets ($n < 10$; Fig. 6), because no random selection of the different traces can be performed and the stacks are still contaminated with seismic noise. Like the bootstrap method, the chi-square estimator technique becomes unstable, if only a small amount of RF traces is available. For a reasonable amount of RFs with a good signal-to-noise ratio ($n > 10$–15) stable models and uncertainties of the model parameters can be derived.

The large database from GEOFON station MLR enabled a detailed study of the RF waveforms including azimuthal variations and permitted a statistically well-founded analysis of the results. The RF section in Fig. 4 shows a clear backazimuthal dependence, expressed by several sharp time shifts of the converted phases from the Moho. The most obvious change in waveform occurs at BAZ ∼70°, where an abrupt time shift from 5.8 s to 4.1 s delay time is observed. It is caused by 3-D lateral variations in crustal structure, and at least two different models can be proposed: An abrupt change of the Moho depth from 45 km depth in NE direction to around 30 km depth in SE direction or the influence of a thick sedimentary basin in the foredeep which generates strong sedimentary multiples that distort the Moho conversion. The former explanation disagrees with the seismic refraction results (Hauser *et al.* 2001), which indicate only a smooth change of the crustal thickness. In Fig. 11 the Moho piercing points (crosses) of the rays related to the 198 RFs (Fig. 4) are plotted together with the sedimentary thickness in the surrounding area of MLR after Martin *et al.* (2005). The dashed lines correspond to the contour lines for basement depths of 0 km, 10 km and 15 km, respectively. The different colours of the crosses represent the BAZ intervals of 315–70°, 70–180° and 180–315°

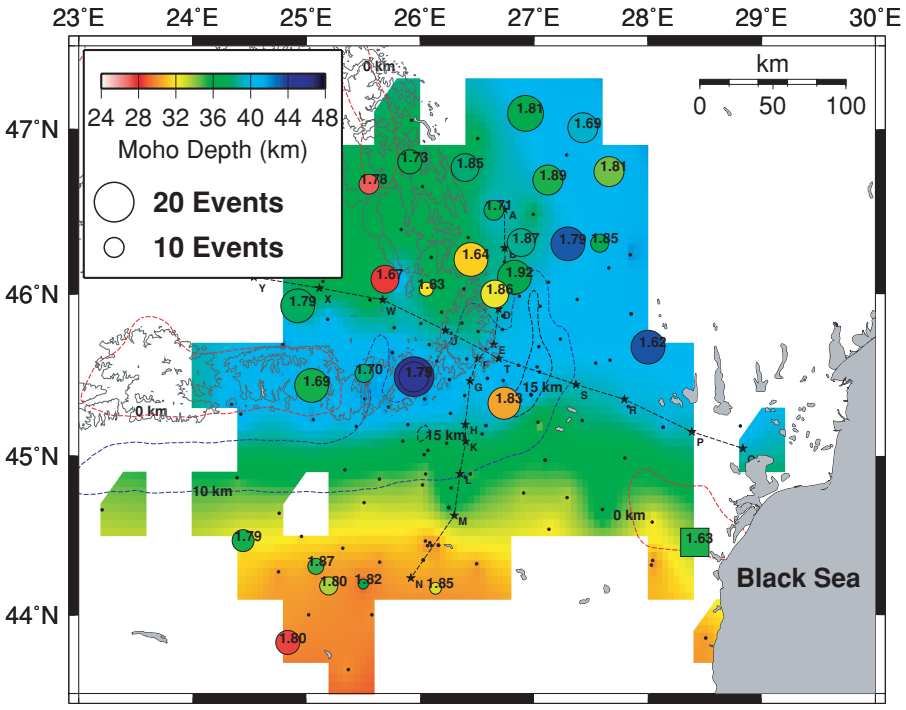

Figure 10. Results of the grid search for Moho depth and v_p/v_s at the 28 CALIXTO99 stations, MLR (coloured circles) and TIRR (coloured square) compared with the Moho model (background) after Martin *et al.* (2005). The diameter of the circles is proportional to the number of used receiver functions. For station TIRR we used 84 events. The values next to the circles give the bootstrap result of the v_p/v_s ratio. Asterisks and letters outline the seismic refraction lines.

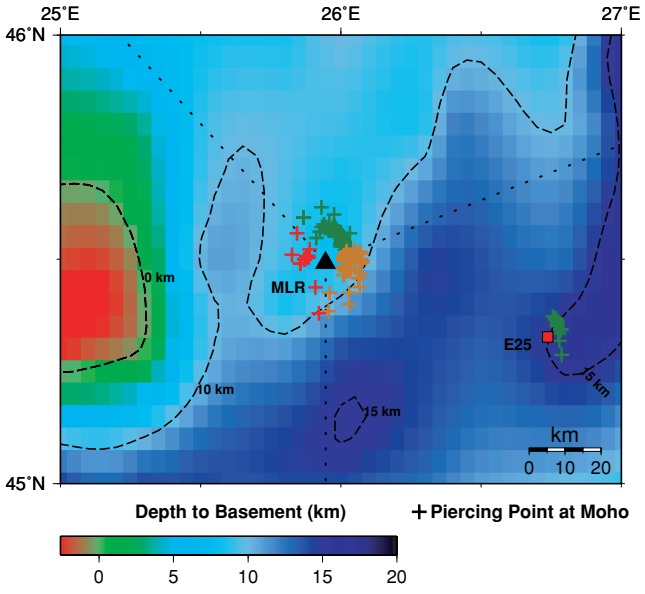

Figure 11. Assumed positions of the piercing points at the Moho for events recorded at station MLR (for the data of Fig. 4) and E25. In addition the depth to the basement is displayed after Martin *et al.* (2005). Depths < 0 km means outcropping crystalline basement. Piercing points for events with BAZ $> 70^\circ$ at MLR are situated in a dipping sedimentary basin.

as mentioned in section 3.1 (dotted lines.) The piercing points with $70^\circ <$ BAZ $< 180^\circ$ clearly correlate with the edge of a depression in the sedimentary foredeep basin. Therefore, we assign the observed time-shift and the azimuthal change of the RF waveforms at MLR to a 3-D effect of the sedimentary structure in the foredeep.

Station E25 is also situated in this region with a strongly dipping basin structure (Fig. 11) where the piercing points lie below a dipping interface. The grid search finds a shallow and prominent conversion interface at around 30 km depth which is too shallow for the Moho and too deep for the upper boundary of the basement. The waveform modelling for station E25 (Fig. 9b) determines the bottom of the nearby sedimentary Focsani basin at about 17 km depth, which is close to the value of about 20 km from seismic refraction modelling (Hauser & Railenau, personal communication, 2004). For this interface, the $H - \kappa$ grid search yields a wrong depth result, since the assumed stacking velocity (mean crustal v_p) is much too high. These examples demonstrate that we have to consider the influence of 3-D crustal structures carefully during the interpretation of the $H - \kappa$ grid-search results.

Fig. 12 summarizes the smoothed basement topography of the whole region. For the four stations shown in Figs 8 and 9, the sedimentary thicknesses are plotted along NS (latitude) and EW (longitude) profiles to highlight the local 3-D structure. As most earthquakes have a BAZ between 0° and 135°, we expect major waveform perturbations due to 3-D structural effects at stations E25 and C03. Respective complicated waveforms are indeed identified by the RF waveform modelling, which leads to complex and ambiguous v_s depth functions for these stations (Fig. 9).

Our main results are presented in Fig. 10 which shows the distribution of the mean $H - \kappa$ grid-search results after the bootstrap analysis (coloured circles). The diameter of the circles is proportional to the number of used RFs. The RF results are compared with the Moho model (background colour) by Martin *et al.* (2005) which is derived mainly from the seismic refraction models, preliminary RF results and interpolation at the CALIXTO99 sites. The numbers next to the station sites denote the κ value determined by the grid search. For most CALIXTO stations in the region of the Carpathian Orogene and the East European Platform we observe a rather good

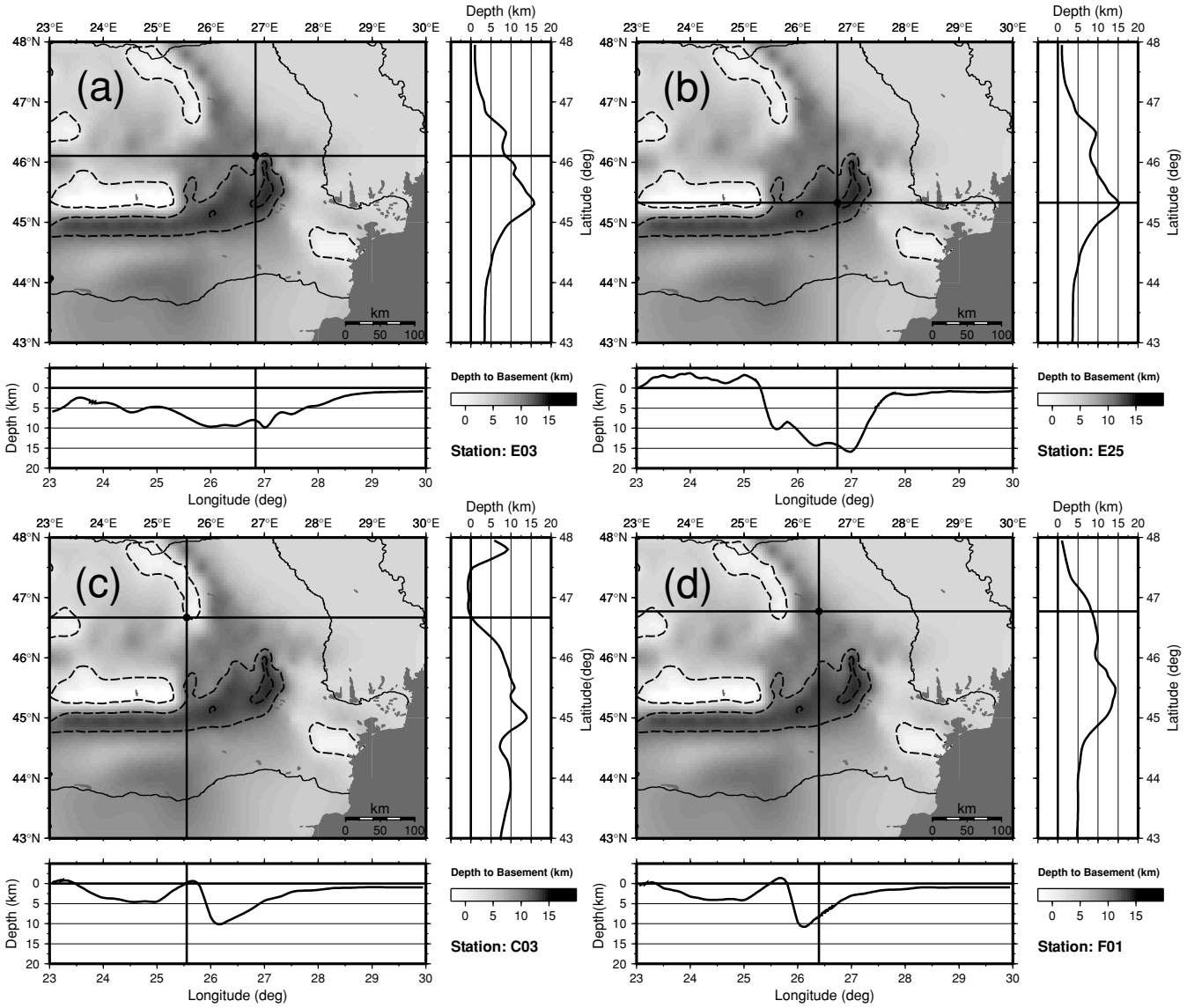

Figure 12. Topography of the basement in SE Romania after Martin *et al.* (2005). Profiles in NS and EW directions through four CALIXTO99 stations sites visualise the complex lateral variations in crustal structure.

agreement with the background Moho depth model. For stations MLR and E21 we obtain the maximum crustal thickness of 45 km in the SE Carpathian Mountains. This is slightly larger than in the seismic refraction model (41 km) which is located to the east. In the SW part of the network the RF results indicate a thicker crust (∼33–35 km) than in the background model. Although the amount of RF data is low in this area, our results should be preferred, because the background model is hardly based on reliable measurements in this area. The RF results at stations in the Transylvanian Basin indicate partly a shallow Moho (28–30 km depth). On the East European platform we find a crustal thickness of 35–39 km in the northern part of the CALIXTO network. Further to the east the Moho descends to 40 km and even 44 km depth. The lack of RF results in the SE part of the network is due to incoherent RF waveforms between different events which may be due to increased cultural noise and reverberations in up to 10-km-thick sediments.

The spatial distribution of κ which corresponds to the average v_p/v_s ratio of the whole crust, shows no significant pattern but rather large variations. Some increased values of more than 1.8 mostly correlate with thick sedimentary layers. This agrees with the seismic refraction model of Raileanu *et al.* (2004, 2005) that has $1.9 < \kappa < 2.1$ in the uppermost sediments along the VRANCEA99 line. However, a further interpretation of our κ results is abandoned, because the average κ over the entire crust is not meaningful due to the influence of the thick sediments.

ACKNOWLEDGMENTS

We thank M. Martin for extensive help with the data handling, W. Geißler for support concerning the calculation of the RFs and X. Yuan for computing programs. Two anonymous reviewers helped to clarify some points in the manuscript. The CALIXTO group involves the following institutions: University of Bucharest (Romania), National Institute for Earth Physics at Bucharest-Magurele (Romania), ETH Zurich (Switzerland), EOST-IPG at Strasbourg (France), INGV Milano (Italy) and University of Karlsruhe (Germany). The mobile stations for the CALIXTO99 experiment were provided by the ETH Zürich, EOST Strasbourg, Milan

University and the Geophysical Instrument Pool at the GeoForschungsZentrum at Potsdam. The Deutsche Forschungsgemeinschaft financed a major part of CALIXTO99 and T D through grant SFB461.

REFERENCES

Bevington, R.P. & Robinson, K., 1992. *Data Reduction and Error Analysis for the Physical Sciences,* 2nd edn. McGraw-Hill, Boston.

Davison, A.C. & Hinkley, D.V., 1997. *Bootstrap Methods and Their Application,* Cambridge University Press, Cambridge.

Dugda, M.T., Nyblade, A.A., Julia, J., Langston, C.A., Ammon, C.J. & Silas, S., 2005. Crustal structure in Ethiopia and Kenya from receiver function analysis: implications for rift development in eastern Africa, *J. geophys. Res.,* **110,** B01303, doi:10.1029/2004JB003065.

Enescu, D., Danchiv, D. & Bala, A., 1992. Lithosphere structure in Romania II. Thickness of the Earth crust. Depth-dependent propagation velocity curves for the P and S waves, *Stud. Cercet. Geol. Geofiz. Geogr. Geofiz.,* **30,** 3–19.

Fan, G., Wallace, T.C. & Zhao, D., 1998. Tomographic imaging of deep velocity structure beneath the Eastern and Southern Carpathians, Romania: implications for continental collision, *J. geophys. Res.,* **103,** 2705–2723.

Fuchs, K. *et al.*, 1979. The Romanian earthquake of March 4. 1977 II. Aftershocks and migration of seismic activity, *Tectonophysics,* **53,** 225–247.

Hanka, W. & Kind, R., 1994. The GEOFON program, *IRIS Newsletter,* **13,** 1–4.

Hauser, F., Raileanu, V., Fielitz, W., Bala, A., Prodehl, C., Polonic, G. & Schulze, A., 2001. VRANCEA99—the crustal structure beneath the southeastern Carpathians and the Moesian Platform from a seismic refraction profile in Romania, *Tectonophysics,* **340,** 233–256.

Hauser, F., Prodehl, C., Landes, M. & the VRANCEA working group, 2002. Seismic experiments target earthquake-prone region in Romania. *Eos Trans. AGU,* **83,** 457, 462–463.

Julià, J. & Mejía, J., 2004. Thickness and v_p/v_s ratio variation in the Iberian crust, *Geophys. J. Int.,* **156,** 59–72.

Kind, R., Kosarev, G.L. & Petersen, N.V., 1995. Receiver functions at the stations of the German Regional Seismic Network (GRSN), *Geophys. J. Int.,* **121,** 191–202.

Kosarev, G., Kind, R., Sobolev, S.V., Yuan, X., Hanka, W. & Oreshin, S., 1999. Seismic evidence for a detached Indian lithospheric mantle beneath Tibet, *Science,* **283,** 1306–1309.

Martin, M., Ritter, J.R.R. & the CALIXTO working group, 2005. High-resolution teleseismic body-wave tomography beneath SE Romania–I. Implications for three-dimensional versus one-dimensional crustal correction strategies with a new crustal velocity model, *Geophys. J. Int.,* **162,** 448–460. doi:10.1111/j.1365–246X.2005.02661.x

Oncescu, M.C. & Bonjer, K.-P., 1997. A note on the depth recurrence and strain release of large Vrancea earthquakes, *Tectonophysics,* **272,** 291–302.

Oncescu, M.C., Bulacu, V., Anghel, M. & Smalbergher, V., 1984. Three-dimensional *P*-wave velocity image under the Carpathian Arc, *Tectonophysics,* **106,** 305–319.

Oncescu, M.C., Bonjer, K.-P. & Rizescu, M., 1999.Weak and strong ground motion of intermediate depth earthquakes from the Vrancea region, in *Vrancea Earthquakes: Tectonics, Hazard and Risk Mitigation,* pp. 27–42, eds. Wenzel, F., Lungu, D. & Novak, O., Kluwer Academic Publishing, Dordrecht.

Plešinger, A., Hellweg, M. & Seidl, D., 1986. Interactive high-resolution polarization analysis of broad-band seismograms, *J. Geophys.,* **59,** 129–139.

Polonic, G., 1996. Structure of the crystalline basement in Romania, *Rev. Roum. Géophisique,* **40,** 57–70.

Raileanu, V., Diaconescu, C. & Radulescu, F., 1994. Characteristics of Romanian lithosphere from deep seismic reflection profiling, *Tectonophysics,* **239,** 165–185.

Raileanu, V., Diaconescu, C., Mateciuc, D. & Diaconescu, M., 1998. Velocity crustal models under the Romanian telemetered seismological observatories, *Romanian Reports in Physics,* **50,** 123–141.

Raileanu, V., Hauser, F., Bala, A., Prodehl, C. & Fielitz, W., 2004.Complex interpretation of P- and *S*-wave velocity models along of Vrancea99 seismic refraction line, in *Earthquake loss estimation and risk reduction,* pp. 201–219, eds. Lungu, D., Wenzel, F., Mouroux, P. & Tojo, I., Independent Film, Bucharest.

Raileanu, V., Bala, A., Hauser, F., Prodehl, C. & Fielitz, W., 2005. Crustal properties from *S*-wave and gravity data along a seismic refraction profile in Romania, *Tectonophysics,* accepted.

Scherbaum, F., 2001. *Of Poles and Zeros, Fundamentals of Digital Seismology,* 2nd edn, Kluwer Academic Publishing, Dordrecht.

Sperner, B., Lorenz, F.P., Bonjer, K.-P., Hettel, S., Müller, B. & Wenzel, F., 2001. Slab break-off - abrupt cut or gradual detachment? New insights from the Vrancea region (SE Carpathians, Romania), *Terra Nova,* **13,** 172–179.

Tichelaar, B.W. & Ruff, L.J., 1989. How good are our best models? Jackknifing, bootstrapping, and earthquake depth, *EOS, Trans. Am. geophys. Un.,* **70,** 593, 605–606.

Vinnik, L., 1977. Detection of waves converted from P to SV in the mantle, *Phys. Earth planet. Inter.,* **15,** 39–45.

Wenzel, F., Achauer, U., Enescu, D., Kissling, E., Russo, R., Mocanu, V. & Musacchio, G. 1998. Detailed look at final stage of plate break-off is target of study in Romania, *EOS, Trans. Am. geophys. Un.,* **79,** 589–594.

Wenzel, F., Lungu, D. & Novak, O. (eds.), 1999. *Vrancea Earthquakes: Tectonics, Hazard and Risk Mitigation,* Kluwer Academic Publishing, Dordrecht.

Wortel, M.J.R. & Spakman, W., 2000. Subduction and slab detachment in the Mediterranean-Carpathian region, *Science,* **290,** 1910–1917.

Yuan, X., Ni, J., Kind, R., Mechie, J. & Sandvol, E., 1997. Lithospheric and upper mantle structure of southern Tibet from a seismological passive source experiment, *J. geophys. Res.,* **102,** 27 491–27 500.

Zhu, L. & Kanamori, H., 2000. Moho depth variation in southern California from teleseismic receiver functions, *J. geophys. Res.,* **105,** 2969–2980.